Cathodic Pulse Breakdown of Anodic Films on Aluminium in Alkaline Silicate Electrolyte – Understanding the Role of Cathodic Half-cycle in AC Plasma Electrolytic Oxidation

Santosh Prasad Sah, Etsushi Tsuji, Yoshitaka Aoki and Hiroki Habazaki*

Division of Materials Chemistry, Faculty of Engineering, Hokkaido University, Sapporo, Hokkaido, 060-8628, Japan

*Corresponding author: Phone & Fax: +81-11-706-6575, e-mail: habazaki@eng.hokudai.ac.jp

Abstract

Sequential anodic and cathodic pulse voltages were applied on anodized Al micro-electrodes in alkaline silicate electrolyte to explore the role of cathodic pulse in AC or bipolar plasma electrolytic oxidation (PEO) process. SEM observation was carried out to observe the sites of anodic and cathodic breakdown and their morphologies. The prior anodic breakdown accelerated the cathodic breakdown at -50 V, and the acceleration was associated with the preferential cathodic breakdown at the anodic breakdown sites. However, the succeeding anodic breakdown during applying anodic pulse of 420 V for 2 ms was highly suppressed at the cathodic breakdown sites.

Keywords: A: aluminium, B: SEM, C: anodic films

1. Introduction

Plasma electrolytic oxidation (PEO), often also referred to as micro-arc oxidation, spark anodizing or micro-plasma oxidation, has attracted recent attention as a surface engineering process of light metals (Al, Mg and Ti) and their alloys to form ceramic coatings [1] . The thickness of the coatings ranges from tens to hundreds of micrometers, and show good thermo-mechanical properties, corrosion resistance and tribological properties [1-14]. The process involves generation of a large number of short-lived microdischarges on the entire substrate surface. The microdischarges, caused by dielectric breakdown of oxide coatings at high voltages, induce rapid heating and cooling of the coatings, forming highly crystalline, often

high-temperature phases. The coatings contain many characteristic discharge channels, with the channels becoming larger with the time of PEO treatment, such that the coatings formed by PEO are essentially porous. Thus, large discharge pores (with diameter larger than 10 μm) connecting the inner coating close to the metal/film interface with the oxide surface, are often found in the PEO coatings. Such large discharges are detrimental for corrosion and wear resistance of the coatings. Destructive discharges are found to be avoided by employing AC or bipolar power supply and proper electrolytes.

Recently, much attention is paid to 'soft' sparking of PEO, which is often observed at a selected AC or bipolar PEO condition with higher cathodic current with respect to the anodic current [15-20]. Under the 'soft' sparking condition, the formation of a relatively dense and uniform coating of ~100 μm thickness is promoted. The 'soft' sparking is characterized by reduction in the rms voltage and greatly reduced acoustic emission and increased emissions from bound-free electron transitions in the optical emission spectrum [15, 16]. Three-layer coatings are usually formed under the 'soft' sparking condition, comprising an outer layer with a highly porous morphology, a relatively thick and dense intermediate layer and an inner thin barrier layer [21]. The transition to the 'soft' sparking on aluminium is also accelerated by the presence of pre-formed anodic porous alumina layer [18, 22]. The recent extensive studies of the PEO process are improving the coating properties, but the key factors that control the PEO process are not yet fully understood.

Since micro-discharges play a crucial role in the growth of PEO coatings, understanding of the factors affecting characteristics of dielectric discharges and resultant morphology of discharge channels is of importance. So far, the 'soft' sparking has been observed only in alkaline silicate electrolyte, and recently, we have reported that electrolyte as well as pulse voltage during single

pulse anodizing influences largely the morphology of discharge channels. In alkaline silicate electrolyte groove-like discharge channels are formed predominantly and healing of discharge pores is promoted in this electrolyte [23].

The 'soft' sparking occurs under AC or bipolar PEO. Further, it is well accepted that dense coatings with less micro-cracks are obtained by AC PEO compared with DC PEO [24]. However, the role of cathodic process in PEO is not yet well understood. In the present study, cathodic breakdown of the anodic oxide films has been examined by applying a single cathodic pulse voltage on a pre-anodized aluminium micro-electrode. The influence of the cathodic breakdown in the succeeding anodic breakdown is also examined for a better understanding the AC PEO process. An aluminium microelectrode is used in this study to reduce the number of discharge events on the entire surface and hence to assist more ready analysis of the breakdown behaviour.

2. Experimental

Highly pure aluminium wire (99.99%, Nilaco Corporation) of 0.2 mm diameter was first anodized up to 450 V in 0.01 mol dm^{-3} ammonium pentaborate electrolyte to cover the entire wire surface by a thick anodic oxide film. Then, the anodized wire was embedded in resin. The embedded aluminium wire was sectioned by ultramicrotomy technique (RMC, MT-7) using a glass knife to expose a clean and relatively flat surface (hereafter denoted as as-polished Al specimen). The specimen was then anodized in alkaline silicate electrolyte of 0.075 mol dm^{-3} Na_2SiO_3 + 0.05 mol dm^{-3} KOH (pH 12.5) to 350 V at a sweep rate of 3.5 V s^{-1} and held at 350 V for 50 s (350 V-anodized Al specimen). Anodic pulse voltage of 420 V with pulse width of 2 ms and cathodic pulse voltage of -50 V with a pulse width of either 10 ms or 1 s were applied solely or in

sequence. The application of the extended cathodic pulse width (1 s), unlike a practical value of 5 or 10 ms, was carried out to visualize the morphological change in anodic oxide film or metal substrate clearly. The voltage waveforms were fed from a Hokuto-Denko, HB-105 function generator to a Chroma, 61501 Programmable AC Source. Current transients were recorded with a sampling time of 0.1 ms using an Agilent 3441A digital multimeter controlled by NI Labview software. The oxide films of selected specimen were chemically stripped out in a mixed solution of 20 g L^{-1} CrO_3 and 45 ml L^{-1} H_3PO_4 at 363 K for 1.8 ks to expose the metal surface. The surface of oxide film as well as metal substrate was observed with JEOL JSM-6500F field-emission electron microscope (SEM).

3. Results

Fig. 1 shows the current transient during applying -50 V pulse voltage for 1 s on the as-polished and 350 V-anodized Al specimens. For the as-polished specimen, the cathodic current increases immediately to ~150 A cm^{-2} and oscillates largely between 2 and 190 A cm^{-2}. Such current oscillations may be associated with the generation of hydrogen gas, which may cover the small electrode surface repeatedly [25]. Such large current fluctuation is a characteristic of the micro-electrode, since such large current fluctuation was not observed for the aluminium specimen of ~1 cm^2 size. When the cathodic pulse voltage is applied to the 350 V-anodized Al specimen, the initial cathodic current is as low as 1 A cm^{-2}, and the cathodic current increase to the order of 10 A cm^{-2}, which may be associated with film breakdown by hydrogen generation [20], occurs after ~120 ms. From the repeated experiments, the time to reach the breakdown for the 350 V-anodized specimens varied between 15 and 250 ms. Therefore, the cathodic breakdown of 350 V-anodized Al by applying -50 V pulse for 10 ms or less (a practical value of cathodic pulse time in actual

PEO) is not possible. The current after breakdown of the anodic film is still low, compared with the as-polished specimen. The breakdown of the anodic film might occur locally, not on entire surface, resulting in the relatively low cathodic current.

Figs. 2a and 2b show the SEM images of the as-polished specimen after application of -50 V for 1 s. In the low magnification image (Fig. 2a), the surface of aluminium micro-electrode, which is surrounded by resin, is uniform and no remarkable features are visible. The high magnification image (Fig. 2b) reveals that the aluminium surface is covered with a nanoporous layer, which is probably composed of a hydrated alumina corrosion product. In contrast, the 350 V-anodized specimen shows locally damaged surface after application of the cathodic pulse (Fig. 2c). Obviously, the anodic film is broken locally and the development of a porous hydrated oxide layer is visible at a breakdown site (Fig. 2d). In other regions, where no breakdown occurred, anodic oxide film is remained with embryo of a porous layer developing due to alkaline nature of the electrolyte used (Fig. 2e).

Fig. 3 shows the current transient during application of 420 V anodic pulse for 2 ms and subsequent -50 V cathodic pulse for 1 s for the 350V-anodized specimen. During anodic pulse the current density is as high as ~100 A cm^{-2}. When the cathodic pulse of -50 V is applied immediately after the anodic pulse of 420 V, high cathodic current of ~-100 A cm^{-2} is observed, which is in contrast to the very low initial current for the specimen without prior anodic pulse (Fig. 1). The result suggests that the film breakdown due to anodic discharges accelerates the cathodic film breakdown. Remarkable cathodic current decrease is observed between 180 and 400 ms during applying the cathodic pulse; this may be also associated with the hydrogen gas generation, which covers the breakdown sites

The surface after anodic pulse of 420 V for 2 ms contains many discharge channels (Fig. 4a). Groove-like discharge channels (Fig. 4b) are predominantly formed under the present condition. The grooves are formed as a consequence of generation of multiple discharges in the region [23]. Pits-like features are visible inside the grooves (Fig. 4c), but the pits may not be penetrated into the metal substrate due to the re-generation of barrier-type anodic oxide after dielectric breakdown.

The similar surface morphology is observed after the subsequent cathodic pulse for 1 s (Fig. 4d). The characteristic morphology of cathodic breakdown (Fig. 2c) is not seen when the prior anodic pulse is applied. Many groove-like discharge channels, generated during the anodic pulse, remains (Fig. 2e), but beneath the pores inside the grooves, indicated by arrows in Fig. 4e, a porous layer, characteristic of the cathodic breakdown, is present (Fig. 4f). The findings clearly indicate that the cathodic breakdown occurs predominantly inside the groove-like discharge channels. The absence of the regions of cathodic breakdown outside the grooves also supports this fact.

The cathodic breakdown at the anodic breakdown sites is also confirmed from the observation of aluminium surface beneath the anodic film. The anodic films were dissolved in a mixed solution of chromic acid and phosphoric acid and then the metal surface was observed by SEM. In the metal surface beneath the groove-like discharge channels shown in Fig. 5a multiple indentations with a size of single indentation of 1 μm or less are present (Fig. 5b). The indentation should be formed as a consequence of dielectric breakdown of the anodic film; local extra-oxidation of aluminium metal proceeds to re-generate anodic oxide to sustain the high applied voltage. The metal surface morphology changes largely after the subsequent cathodic pulse. Fig. 5d is the metal surface after chemical dissolution of anodic film shown in Fig. 5c. The

cathodic pulse changes the multiple indentations developed during anodic pulse to large craters of several micrometers in size. From the images shown in Figs. 5d and 5e it is likely that the craters appear to develop due to faceted dissolution of aluminium during applying cathodic pulse for 1 s.

Next, the influence of the cathodic pulse on the anodic discharge during the succeeding anodic pulse has been examined. Fig. 6a shows a current transient during the sequential anodic pulse (420 V, 2 ms)/cathodic pulse (-50 V, 1 s)/anodic pulse (420 V, 2 ms). For comparison, the current transient during two anodic pulses of 420 V for 2 ms with intermission for 1 s is revealed (Fig. 6b). Comparable anodic currents are obtained for the 1^{st} and 2^{nd} anodic pulses when no cathodic voltage is applied. From the repeated experiments of more than four times, the electric charge passed during the first anodic pulse is 139 ± 19 mC cm^{-2} while that during the second anodic pulse is 171 ± 20 mC cm^{-2}. In contrast, when the cathodic pulse of 1 s is applied, the current during the second anodic pulse is almost one order of magnitude lower than that during the first anodic pulse (Fig. 6a). The electric charge is also reduced from 139 ± 19 mC cm^{-2} for the first anodic pulse to 15 ± 5 mC cm^{-2} for the second anodic pulse. Therefore, the cathodic pulse affects largely the succeeding anodic discharge. When the cathodic pulse time was reduced to 10 ms, the current during the second anodic pulse increased, and the electric charge during the second anodic pulse is approximately 0.58 ± 0.09 of that during the first anodic pulse. Thus, even for the short cathodic pulse, the anodic discharges during the succeeding anodic pulse are suppressed to some extent.

Surface observations after the second anodic pulse reveal that larger discharge channels of ~35 μm in size are developed, as indicated arrows in Fig. 7b, after the second anodic pulse with the intermission for 1 s, while the size of the discharge channels of 15 μm or less is maintained even

after the second anodic pulse with cathodic pulse (Fig. 7a). During the second anodic pulse after the intermission for 1 s, the dielectric breakdown appears to occur preferentially in the groove-like discharge channels developed during the first anodic pulse, enlarging the discharge channels. When the cathodic pulse is applied between two anodic pulses, no such large discharge channels are absent. The discharge channels formed during the first anodic pulse appear to become more resistive for the succeeding anodic breakdown after the cathodic breakdown, leading to the remarkable reduction of the current during the second anodic pulse. When the second anodic pulse of 300 V was applied after the cathodic pulse, a porous layer in the discharge channels (Fig. 8a and 8b) changed to an apparently non-porous layer. Since no anodic breakdown occurs at this anodic voltage, this non-porous layer is developed by usual growth of anodic oxide without dielectric breakdown. Even when the second anodic pulse of 420 V is applied, similar non-porous oxide layer is found in the discharge channels (upper-right discharge channel of Fig. 8c and 8d). In addition, new discharge channels are developed during the second anodic pulse, as indicated by an arrow in Fig. 8c.

4. Discussion

The findings obtained in the present study should be of importance for understanding the AC PEO of aluminium and its alloys. Relatively large discharge pores are usually developed in the PEO coatings and the pore size increases with thickening of the coatings [27]. However, if the 'soft' sparking condition is established, relatively compact and thick intermediate layer develops, although an outer layer is still rather rough and highly porous [21]. The 'soft' sparking has been reported only in alkaline silicate electrolyte for aluminium and its alloys. Further, larger cathodic

current with respect to the anodic current in AC or bipolar PEO is one of the essential requisites for ‘soft’ sparking. Thus, the cathodic process should have a crucial role in establishing the ‘soft’ sparking condition in AC PEO.

The present study reveals that the cathodic breakdown is accelerated by the presence of anodic discharge channels developed by dielectric breakdown of an anodic film at high anodic pulse voltage. The acceleration is associated with the preferential cathodic breakdown at the anodic breakdown sites, where groove-like discharge channels are mainly formed. This means that the anodic film re-generated at the anodic breakdown sites during anodic pulse is less resistive for cathodic breakdown than the regions where no breakdown occurs. This is true even for the second anodic breakdown such that discharge channels of enlarged sizes are developed during the second anodic pulse when no cathodic pulse applies between two anodic pulses. The formation of less-protective film at the anodic breakdown sites must be electrolyte-dependent; in ammonium pentaborate electrolyte, a more resistive film is re-generated at the anodic breakdown sites [23].

It has been reported that an anodic film is locally broken due to hydrogen gas generation beneath the anodic film during cathodic polarization [28]. It is generally hypothesized that such cathodic breakdown may introduce the sites for next anodic breakdown. However, an opposite result is obtained in the present study. Although the anodic breakdown sites are less protective, the sites change to be more protective after the cathodic breakdown, such that anodic dielectric breakdown in the succeeding anodic pulse occurs preferentially in the regions where no prior breakdown occurs. Improved protectiveness of the cathodic breakdown sites avoids the repeated breakdown at the same sites, which induce the generation of large discharge pores. The cathodic breakdown in the silicate electrolytes can thus randomize the anodic breakdown sites, probably

contributing to the formation of more uniform PEO coatings in this electrolyte. The suppression of the anodic breakdown in the succeeding anodic pulse was remarkable when relatively long cathodic pulse width was applied. Such breakdown behaviour in sequential anodic and cathodic pulse voltages is schematically illustrated in Fig. 9. The present finding on the effective suppression of anodic breakdown after the longer cathodic pulse may also be correlated to the requisite of the higher cathodic current with respect to the anodic current for establishing the 'soft' sparking.

5. Conclusions

1. Cathodic breakdown of anodic film on aluminium in alkaline silicate electrolyte at -50 V occurs preferentially at the prior anodic breakdown sites, since less-protective oxide layer is probably present at the anodic discharge sites.
2. At the cathodic breakdown sites a characteristic nanoporous layer, probably composed of hydrated alumina, is developed.
3. The second anodic breakdown is significantly suppressed by the preceding cathodic breakdown. The nanoporous layer at the cathodic breakdown sites changes to a compact non-porous oxide layer, which is more resistive for anodic breakdown than the regions where no breakdown occurs. Thus, the cathodic breakdown can randomize the sites of succeeding anodic breakdown and avoid repeated breakdown at the same sites and formation of large discharge channels.

Acknowledgements

The present work was supported in part by Grant-in-Aids for Scientific Research (A) No. 19206077 from the Japan Society for the Promotion of Science, the Light Metal Educational Foundation, Inc. and the Global COE Program (Project No. B01: Catalysis as the Basis for Innovation in Materials Science) from the Ministry of Education, Culture, Sports, Science and Technology (MEXT), Japan.

References

[1] A.L. Yerokhin, X. Nie, A. Leyland, A. Matthews, S.J. Dowey, Plasma electrolysis for surface engineering, Surf. Coat. Technol., 122 (1999) 73-93.

[2] J. Tian, Z.Z. Luo, S.K. Qi, X.J. Sun, Structure and antiwear behavior of micro-arc oxidized coatings on aluminum alloy, Surf. Coat. Technol., 154 (2002) 1-7.

[3] J.A. Curran, T.W. Clyne, Thermo-physical properties of plasma electrolytic oxide coatings on aluminium, Surf. Coat. Technol., 199 (2005) 168-176.

[4] X.T. Sun, Z.H. Jiang, S.G. Xin, Z.P. Yao, Composition and mechanical properties of hard ceramic coating containing α-Al_2O_3 produced by microarc oxidation on ti-6al-4v alloy, Thin Solid Films, 471 (2005) 194-199.

[5] T.B. Wei, F.Y. Yan, J. Tian, Characterization and wear- and corrosion-resistance of microarc oxidation ceramic coatings on aluminum alloy, J. Alloys Compd., 389 (2005) 169-176.

[6] H.P. Duan, K.Q. Du, C.W. Yan, F.H. Wang, Electrochemical corrosion behavior of composite coatings of sealed mao film on magnesium alloy AZ91D, Electrochim. Acta, 51 (2006) 2898-2908.

[7] R. Arrabal, E. Matykina, F. Viejo, P. Skeldon, G.E. Thompson, Corrosion resistance of WE43 and AZ91D magnesium alloys with phosphate PEO coatings, Corros. Sci., 50 (2008) 1744-1752.

[8] P.B. Srinivasan, C. Blawert, W. Dietzel, Effect of plasma electrolytic oxidation treatment on the corrosion and stress corrosion cracking behaviour of AM50 magnesium alloy, Mater. Sci. Eng. A, 494 (2008) 401-406.

[9] D.Y. Hwang, Y.A. Kim, D.H. Shin, Corrosion resistance of plasma-anodized AZ91 Mg alloy in the electrolyte with/without potassium fluoride, Mater. Trans., 50 (2009) 671-678.

[10] P.B. Srinivasan, J. Liang, C. Blawert, M. Stormer, W. Dietzel, Effect of current density on the microstructure and corrosion behaviour of plasma electrolytic oxidation treated AM50 magnesium alloy, Appl. Surf. Sci., 255 (2009) 4212-4218.

[11] H.A. Chen, G.H. Lv, G.L. Zhang, H. Pang, X.Q. Wang, H. Lee, S.Z. Yang, Corrosion performance of plasma electrolytic oxidized AZ31 magnesium alloy in silicate solutions with different additives, Surf. Coat. Technol., 205 (2010) S32-S35.

[12] W.H. Song, Y.K. Jun, Y. Han, S.H. Hong, Biomimetic apatite coatings on micro-arc oxidized titania, Biomaterials, 25 (2004) 3341-3349.

[13] H. Habazaki, T. Onodera, K. Fushimi, H. Konno, K. Toyotake, Spark anodizing of β-Ti alloy for wear-resistant coating, Surf. Coat. Technol., 201 (2007) 8730-8737.

[14] S. Tsunekawa, Y. Aoki, H. Habazaki, Two-step plasma electrolytic oxidation of Ti-15V-3Al-3Cr-3Sn for wear-resistant and adhesive coating, Surf. Coat. Technol., 205 (2011) 4732-4740.

[15] F. Jaspard-Mecuson, T. Czerwiec, G. Henrion, T. Belmonte, L. Dujardin, A. Viola, J. Beauvir, Tailored aluminium oxide layers by bipolar current adjustment in the plasma electrolytic oxidation (PEO) process, Surf. Coat. Technol., 201 (2007) 8677-8682.

[16] A.I. Slonova, O.P. Terleeva, Morphology, structure, and phase composition of microplasma coatings formed on Al-Cu-Mg alloy, Protect. Met., 44 (2008) 65-75.

[17] R. Arrabal, E. Matykina, T. Hashimoto, P. Skeldon, G.E. Thompson, Characterization of AC PEO coatings on magnesium alloys, Surf. Coat. Technol., 203 (2009) 2207-2220.

[18] E. Matykina, R. Arrabal, A. Mohamed, P. Skeldon, G.E. Thompson, Plasma electrolytic oxidation of pre-anodized aluminium, Corros. Sci., 51 (2009) 2897-2905.

[19] E. Matykina, R. Arrabal, D.J. Scurr, A. Baron, P. Skeldon, G.E. Thompson, Investigation of the mechanism of plasma electrolytic oxidation of aluminium using O-18 tracer, Corros. Sci., 52 (2010) 1070-1076.

[20] E. Matykina, R. Arrabal, P. Skeldon, G.E. Thompson, Optimisation of the plasma electrolytic oxidation process efficiency on aluminium, Surf. Interface Anal., 42 (2010) 221-226.

[21] E. Matykina, R. Arrabal, P. Skeldon, G.E. Thompson, Investigation of the growth processes of coatings formed by ac plasma electrolytic oxidation of aluminium, Electrochim. Acta, 54 (2009) 6767-6778.

[22] E. Matykina, R. Arrabal, P. Skeldon, G.E. Thompson, P. Belenguer, AC PEO of aluminium with porous alumina precursor films, Surf. Coat. Technol., 205 (2010) 1668-1678.

[23] S.P. Sah, Y. Tatsuno, Y. Aoki, H. Habazaki, Dielectric breakdown and healing of anodic oxide films on aluminium under single pulse anodizing, Corros. Sci., 53 (2011) 1838-1844.

[24] S. Xin, L. Song, R. Zhao, X. Hu, Influence of cathodic current on composition, structure and properties of Al_2O_3 coatings on aluminum alloy prepared by micro-arc oxidation process, Thin Solid Films, 515 (2006) 326-332.

[25] P. Kristof, M. Pritzker, Effect of electrolyte composition on the dynamics of hydrogen gas bubble evolution at copper microelectrodes, J. Appl. Electrochem., 27 (1997) 255-265.

[26] A.R. Despic, J. Radosevic, P. Dabic, M. Kliskic, Abnormal yields of hydrogen and the mechanism of its evolution during cathodic polarization of aluminum, Electrochim. Acta, 35 (1990) 1743-1746.

[27] E. Matykina, A. Berkani, P. Skeldon, G.E. Thompson, Real-time imaging of coating growth during plasma electrolytic oxidation of titanium, Electrochim. Acta, 53 (2007) 1987-1994.

[28] H. Takahashi, K. Fujiwara, M. Seo, The cathodic polarization of aluminum covered with anodic oxide-films in a neutral borate solution .2. Film breakdown and pit formation, Corros. Sci., 36 (1994) 689-705.

Figure caption

Fig. 1 : Current transients of the as-polished and 350 V-anodized Al micro-electrodes during applying cathodic pulse of -50 V for 1 s in 0.075 mol dm^{-3} Na_2SiO_3+0.05 mol dm^{-3} KOH at 293 K.

Fig. 2 SEM images of (a, b) the as-polished and (c, d, e) 350 V-anodized Al micro-electrodes after applying cathodic pulse of -50 V for 1 s in 0.075 mol dm^{-3} Na_2SiO_3+0.05 mol dm^{-3} KOH at 293 K.

Fig. 3 Current transient of the 350-V anodized Al micro-electrode during sequential anodic (420 V for 2 ms)/cathodic (-50 V for 1 s) pulses in 0.075 mol dm^{-3} Na_2SiO_3+0.05 mol dm^{-3} KOH at 293 K.

Fig. 4 SEM images of the 350-anodized Al micro-electrode after (a, b, c) anodic pulse of 420 V for 2 ms and (d, e, f) sequential anodic (420 V for 2 ms)/cathodic (-50 V for 1 s) pulses in 0.075 mol dm^{-3} Na_2SiO_3+0.05 mol dm^{-3} KOH at 293 K.

Fig. 5 SEM images of (a, c) oxide and (b, d, e) metal surfaces of the 350-anodized Al micro-electrode after (a, b) anodic pulse of 420 V for 2 ms and (c, d, e) sequential anodic (420 V for 2 ms)/cathodic (-50 V for 1 s) pulses in 0.075 mol dm^{-3} Na_2SiO_3+0.05 mol dm^{-3} KOH at 293 K.

Fig. 6 Current transients of the 350-anodized Al micro-electrode during sequential (a) anodic (420 V for 2 ms)/cathodic (-50 V for 1 s)/anodic (420 V for 2ms) pulses and (b) anodic (420 V for 2 ms)/intermission (1 s) /anodic (420 V for 2ms) pulses in 0.075 mol dm^{-3} Na_2SiO_3+0.05 mol dm^{-3} KOH at 293 K.

Fig. 7 SEM images of the 350-anodized Al micro-electrode after sequential (a) anodic (420 V for 2 ms)/cathodic (-50 V for 1 s)/anodic (420 V for 2ms) pulses and (b) anodic (420 V for 2 ms)/intermission (1 s) /anodic (420 V for 2ms) pulses in 0.075 mol dm^{-3} Na_2SiO_3+0.05 mol dm^{-3} KOH at 293 K.

Fig. 8 SEM images of the 350-anodized Al micro-electrode after sequential (a) anodic (420 V for 2 ms)/cathodic (-50 V for 1 s)/anodic (300 V for 2ms) pulses and (b) anodic (420 V for 2 ms)/cathodic (-50 V for 1 s)/anodic (420 V for 2ms) pulses in 0.075 mol dm^{-3} Na_2SiO_3+0.05 mol dm^{-3} KOH at 293 K.

Fig. 9 Schematic illustration showing the breakdown sites during sequential anodic and cathodic pulses.

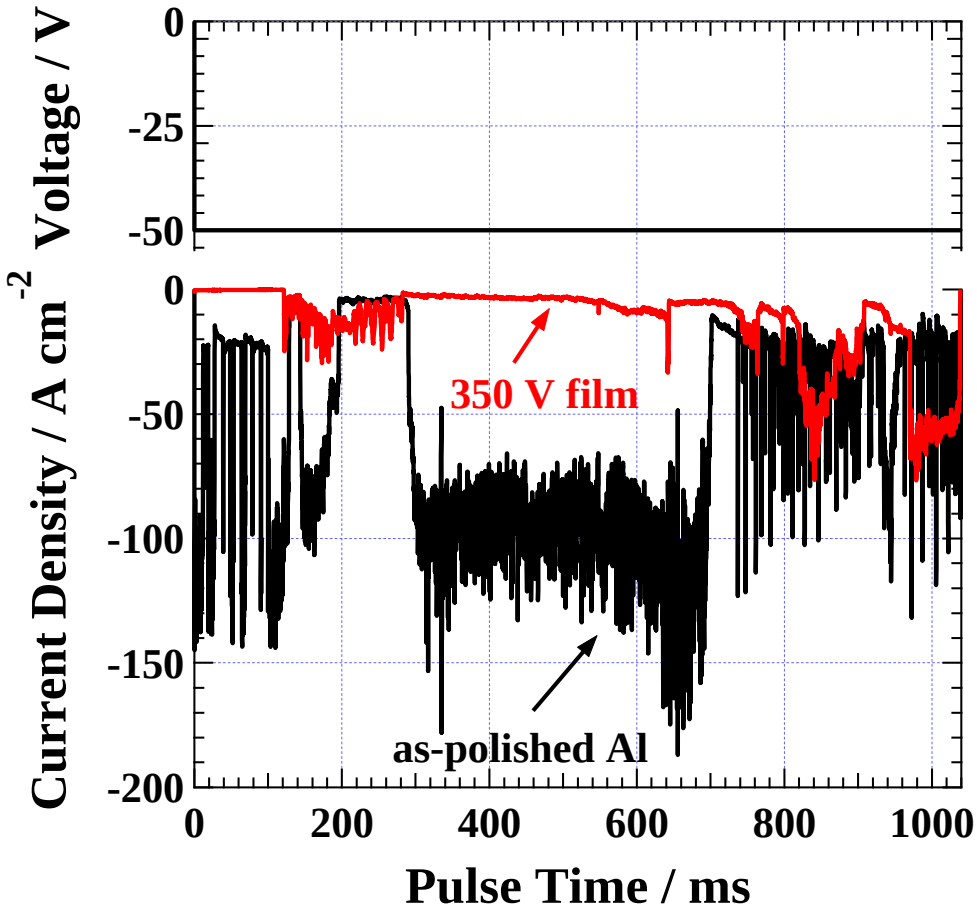
Voltage / V
0
-25
-50
Current Density / A cm-2
0
-50
-100
-150
-200
350 V film
as-polished Al
0
200
400
600
800
1000
Pulse Time / ms

Fig. 1

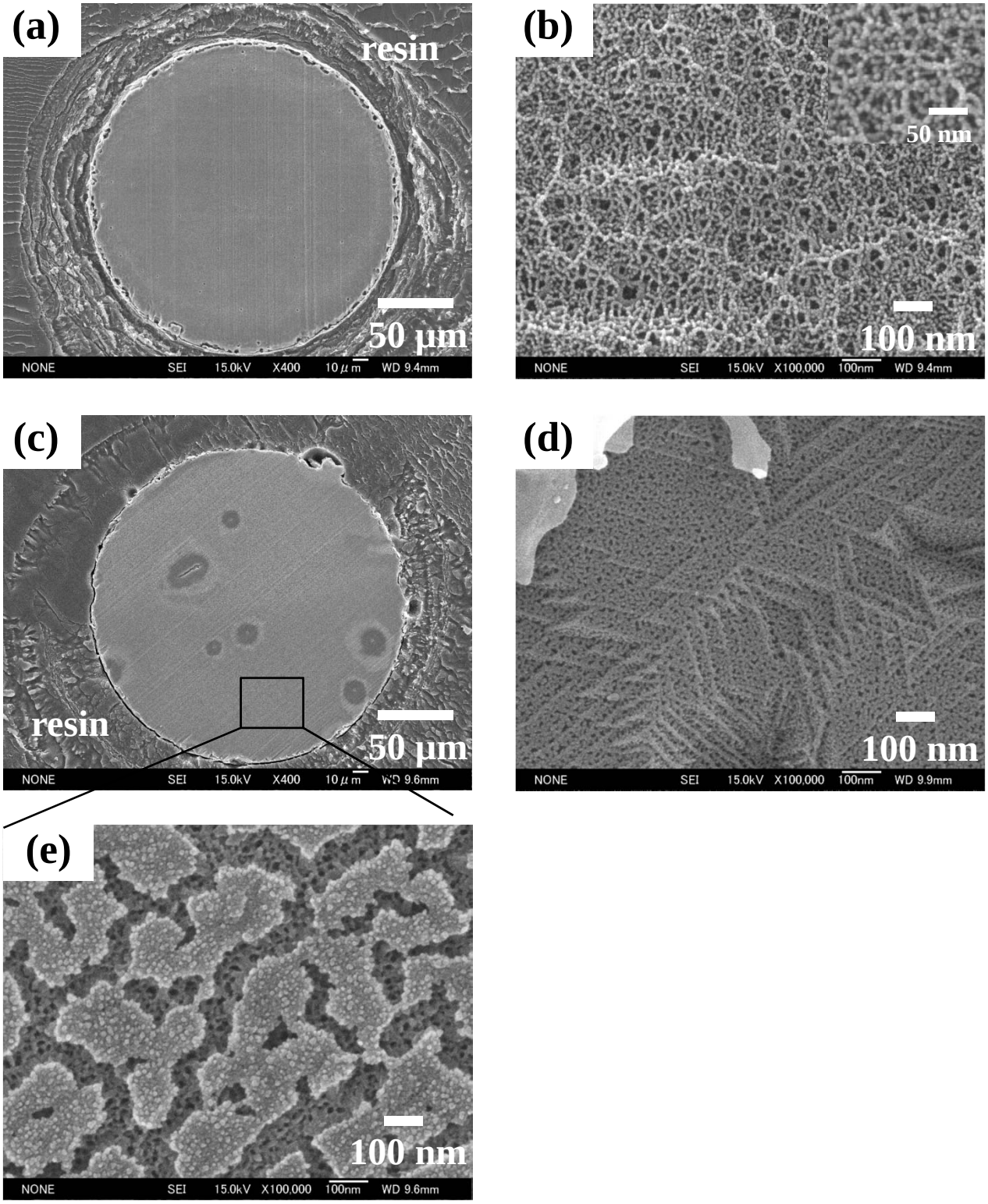
(a)
resin
50 µm
NONE SEI 15.0kV X400 10µm WD 9.4mm
(b)
50 nm
100 nm
NONE SEI 15.0kV X100,000 100nm WD 9.4mm
(c)
resin
50 µm
NONE SEI 15.0kV X400 10µm WD 9.6mm
(d)
100 nm
NONE SEI 15.0kV X100,000 100nm WD 9.9mm
(e)
100 nm
NONE SEI 15.0kV X100,000 100nm WD 9.6mm

Fig. 2

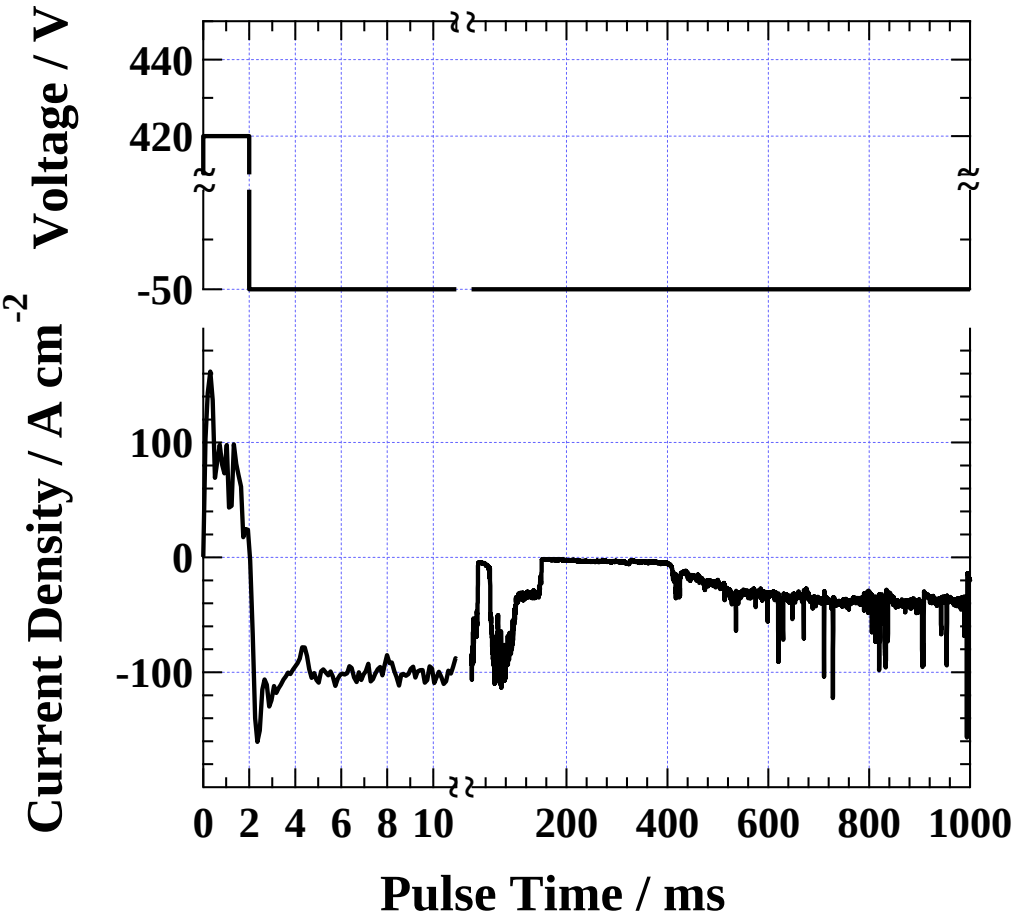
Voltage / V
440
420
-50
Current Density / A cm-2
100
0
-100
0 2 4 6 8 10 200 400 600 800 1000
Pulse Time / ms

Fig. 3

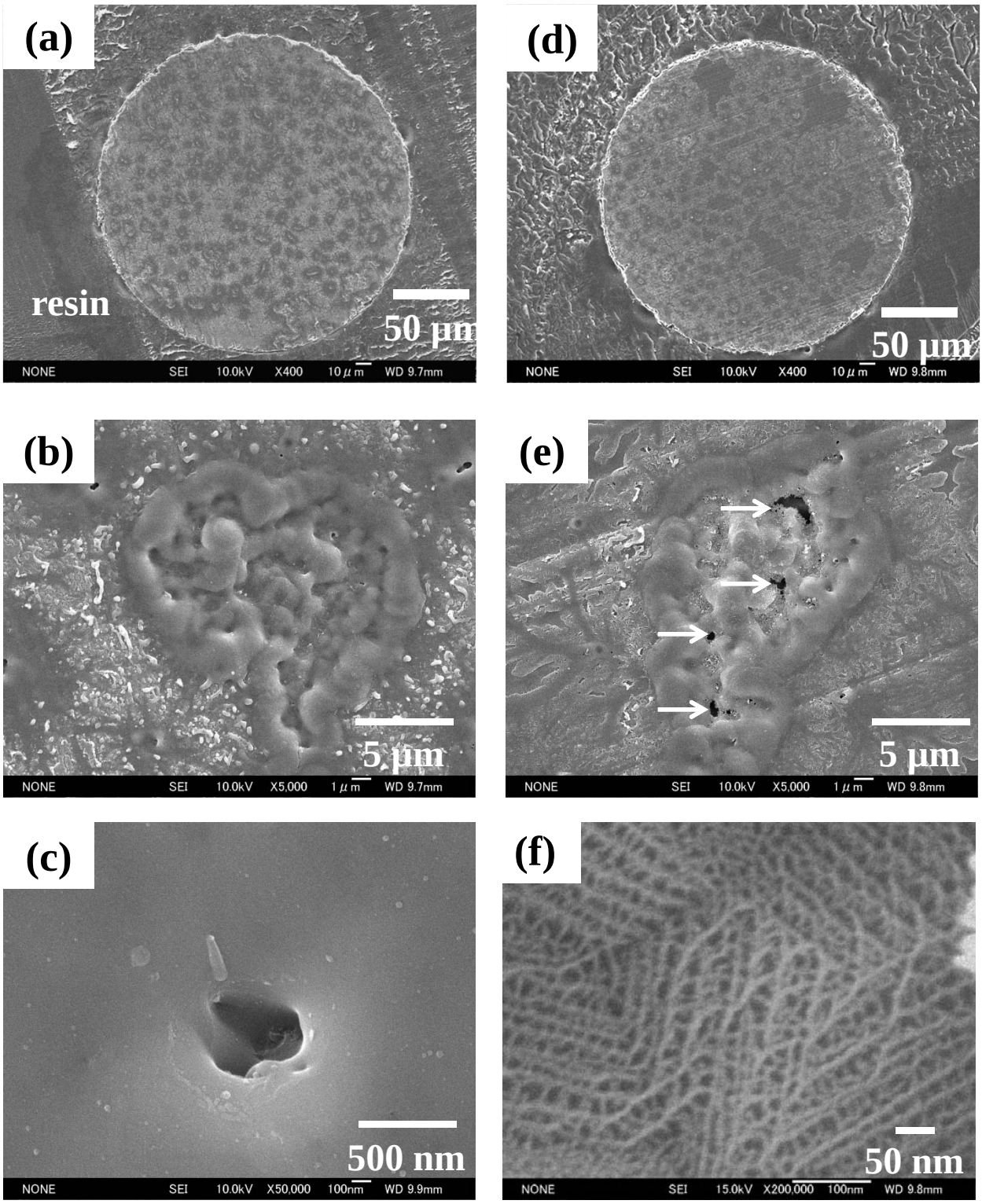
(a)
resin
50 µm
NONE SEI 10.0kV X400 10µm WD 9.7mm
(d)
50 µm
NONE SEI 10.0kV X400 10µm WD 9.8mm
(b)
5 µm
NONE SEI 10.0kV X5,000 1µm WD 9.7mm
(e)
5 µm
NONE SEI 10.0kV X5,000 1µm WD 9.8mm
(c)
500 nm
NONE SEI 10.0kV X50,000 100nm WD 9.9mm
(f)
50 nm
NONE SEI 15.0kV X200,000 100nm WD 9.8mm

Fig. 4

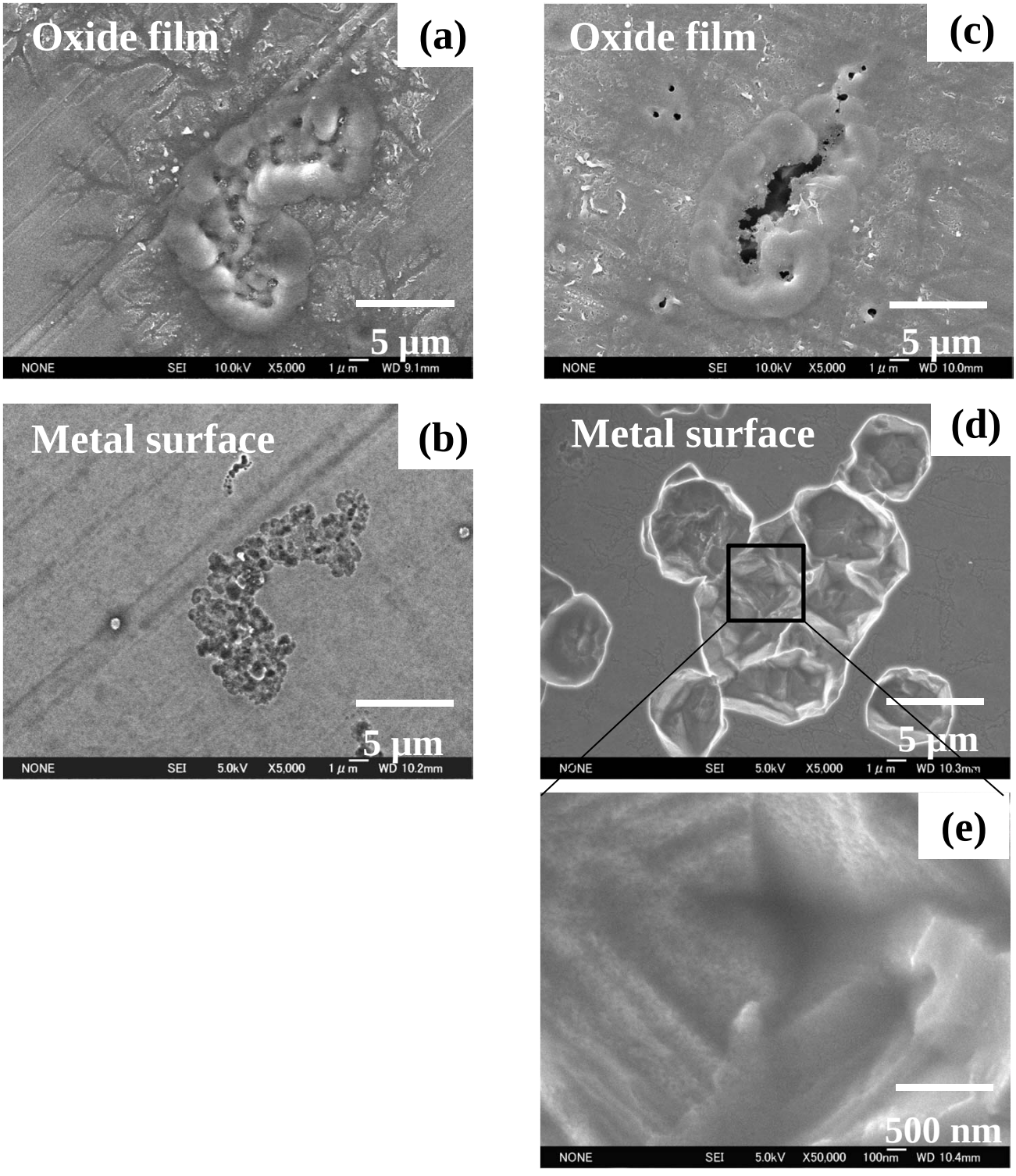
Oxide film
(a)
5 µm
NONE SEI 10.0kV X5,000 1 µm WD 9.1mm
Oxide film
(c)
5 µm
NONE SEI 10.0kV X5,000 1 µm WD 10.0mm
Metal surface
(b)
5 µm
NONE SEI 5.0kV X5,000 1 µm WD 10.2mm
Metal surface
(d)
5 µm
NONE SEI 5.0kV X5,000 1 µm WD 10.3mm
(e)
500 nm
NONE SEI 5.0kV X50,000 100nm WD 10.4mm

Fig. 5

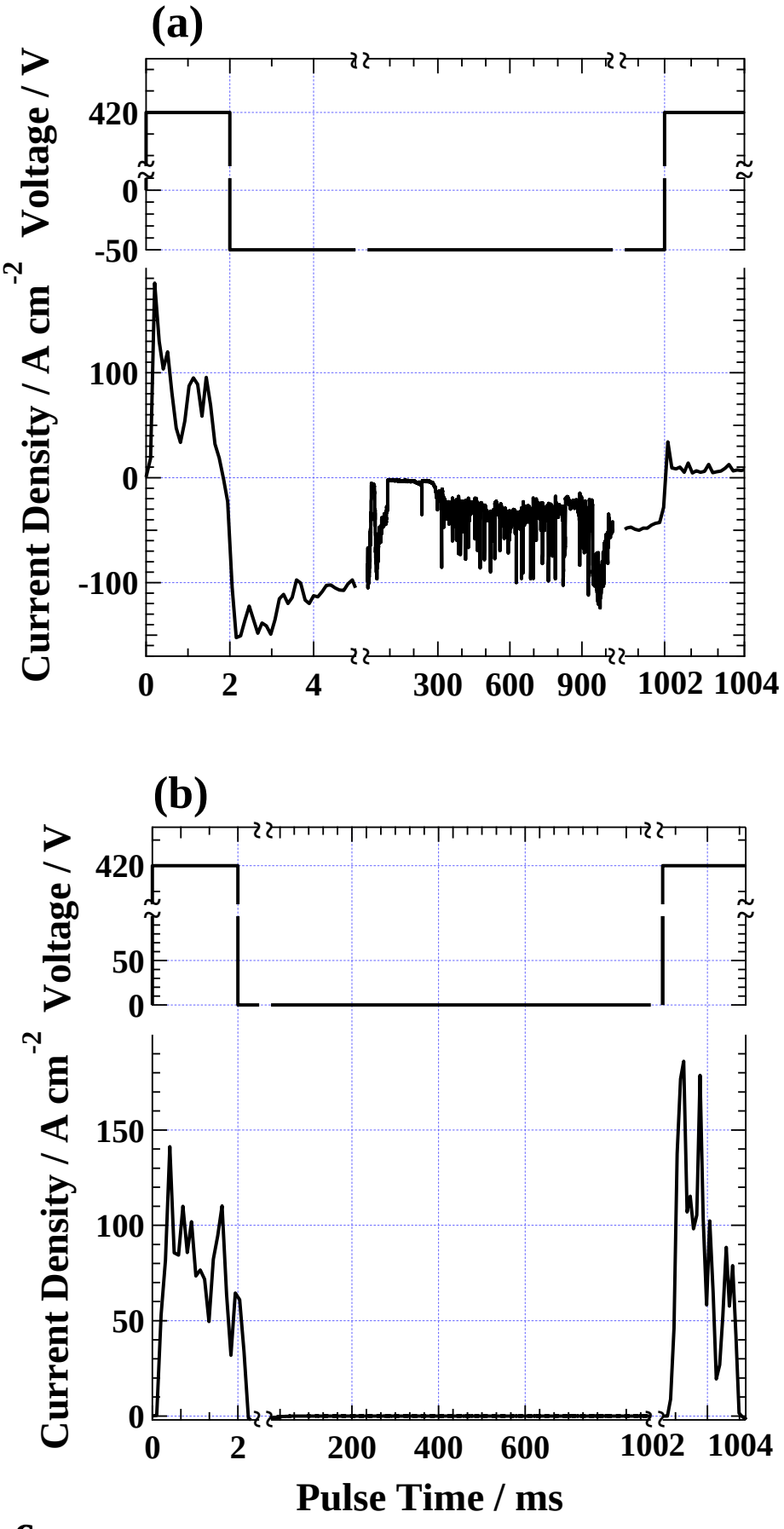
(a)
Voltage / V
420
0
-50
Current Density / A cm-2
100
0
-100
0
2
4
300
600
900
1002
1004
(b)
Voltage / V
420
50
0
Current Density / A cm-2
150
100
50
0
0
2
200
400
600
1002
1004
Pulse Time / ms

Fig. 6

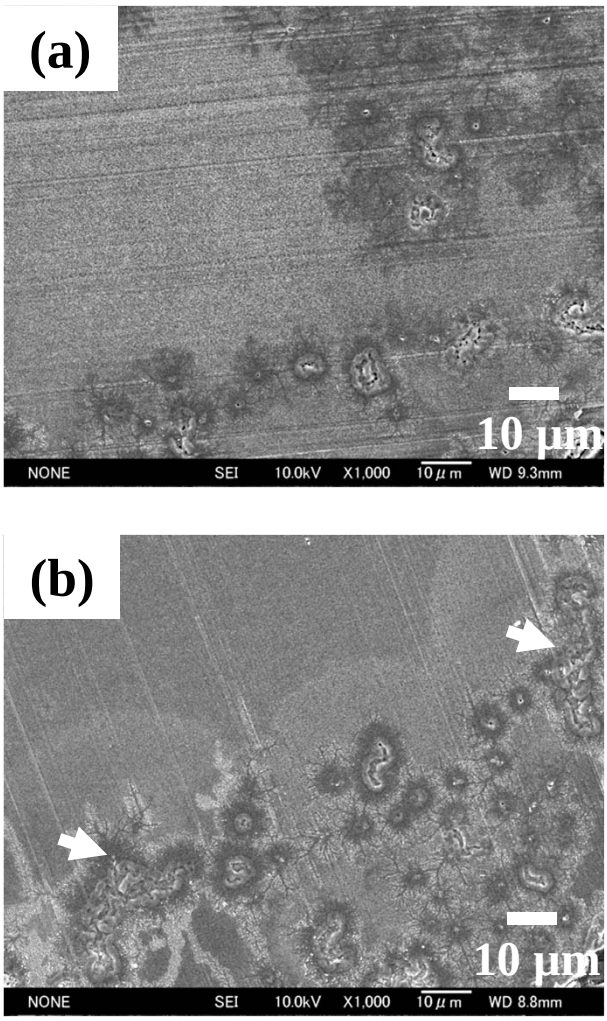
(a)
10 μm
NONE SEI 10.0kV X1,000 10μm WD 9.3mm
(b)
10 μm
NONE SEI 10.0kV X1,000 10μm WD 8.8mm

Fig. 7

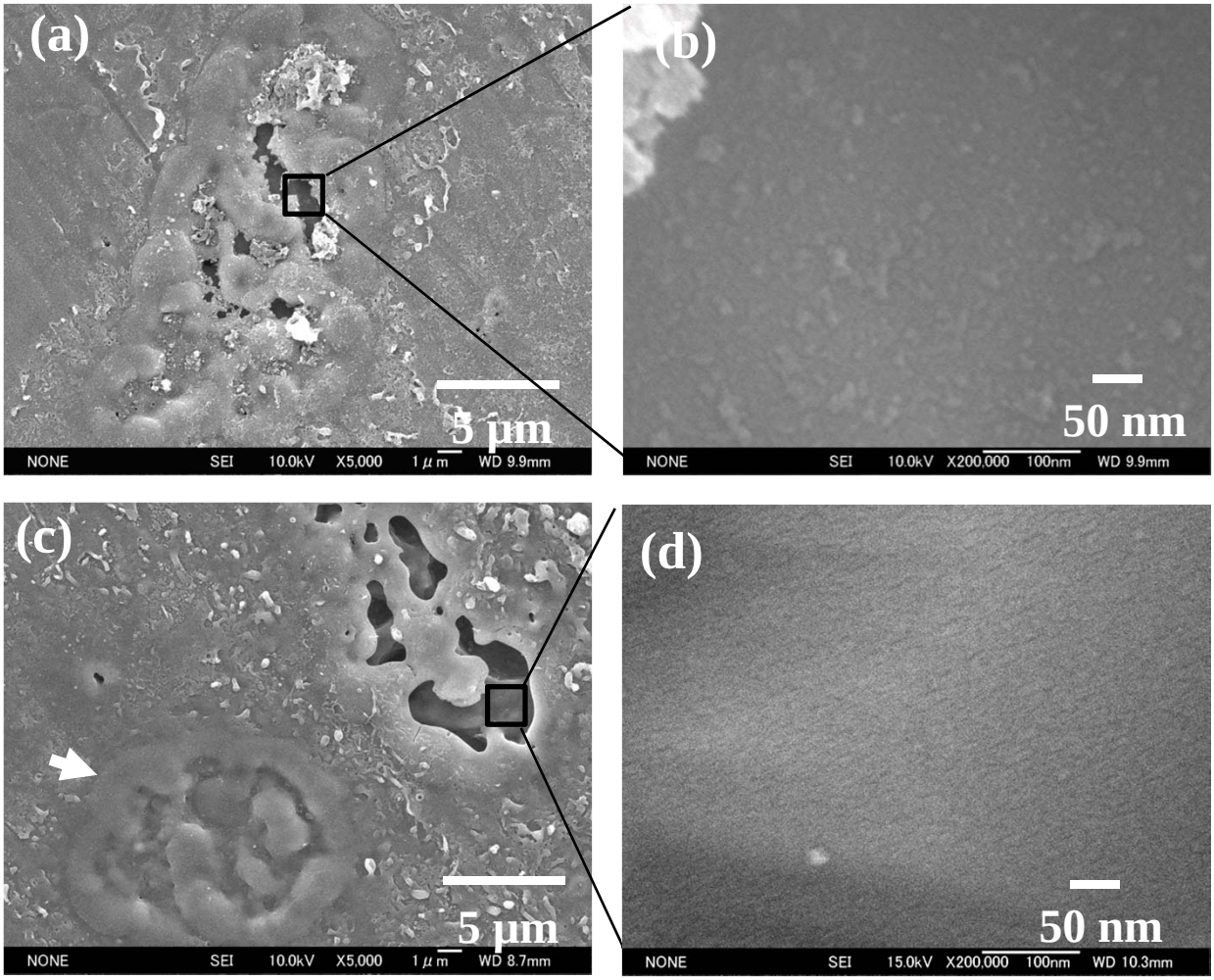
(a)
5 µm
NONE SEI 10.0kV X5,000 1 µm WD 9.9mm
(b)
50 nm
NONE SEI 10.0kV X200,000 100nm WD 9.9mm
(c)
5 µm
NONE SEI 10.0kV X5,000 1 µm WD 8.7mm
(d)
50 nm
NONE SEI 15.0kV X200,000 100nm WD 10.3mm

Fig. 8

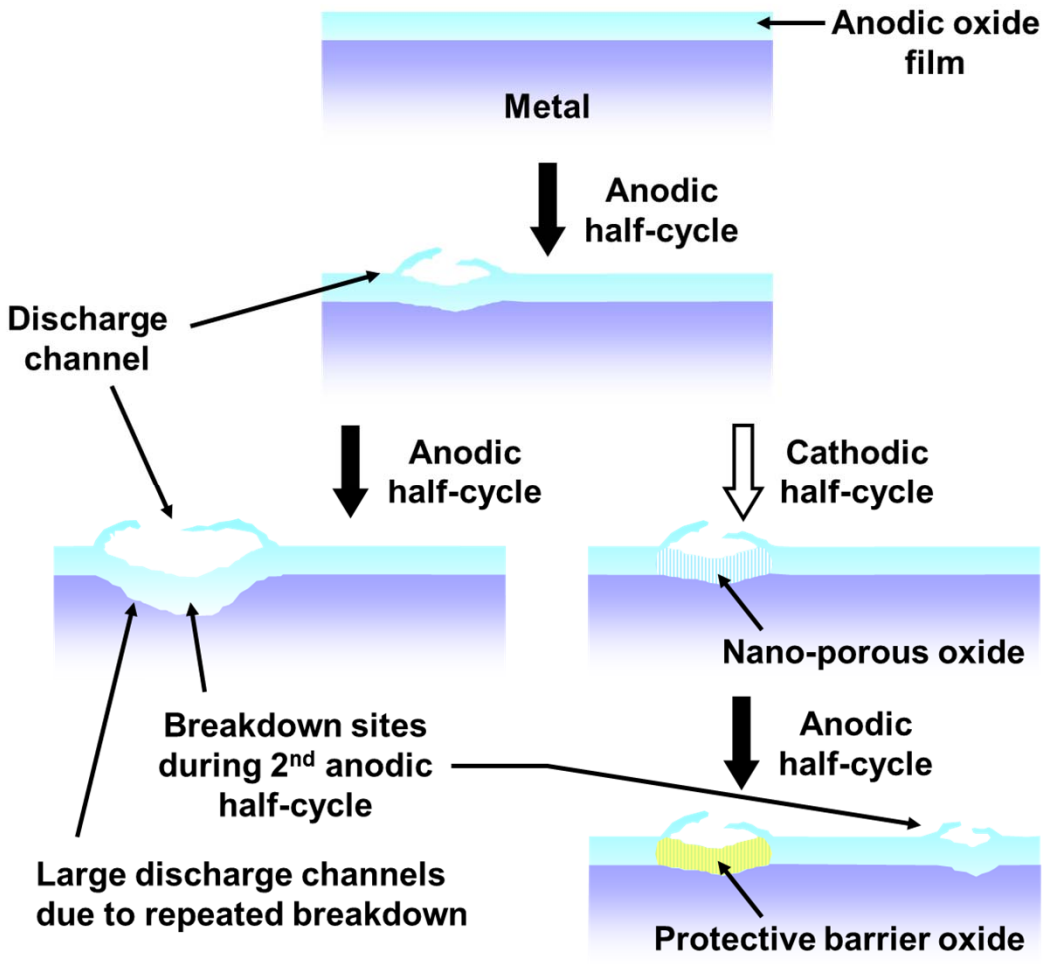
Anodic oxide film
Metal
Anodic half-cycle
Discharge channel
Anodic half-cycle
Cathodic half-cycle
Nano-porous oxide
Breakdown sites during 2nd anodic half-cycle
Anodic half-cycle
Large discharge channels due to repeated breakdown
Protective barrier oxide

Fig. 9